



# Molecular scissor tailoring hierarchical architecture of ZIF-derived Fe/N/C catalysts for acidic oxygen reduction reaction

Yangyang Liu<sup>a,b</sup>, Fengdi Tu<sup>b</sup>, Ziyu Zhang<sup>b</sup>, Zigang Zhao<sup>a,b</sup>, Pan Guo<sup>b</sup>, Lixiao Shen<sup>a,b</sup>, Yunlong Zhang<sup>b,\*</sup>, Lei Zhao<sup>b,\*</sup>, Guangjie Shao<sup>a,\*</sup>, Zhenbo Wang<sup>b,\*</sup>

<sup>a</sup> State Key Laboratory of Metastable Materials Science and Technology, Hebei Key Laboratory of Applied Chemistry, College of Environmental and Chemical Engineering, Yanshan University, Qinhuangdao 066004, PR China

<sup>b</sup> MIIT Key Laboratory of Critical Materials Technology for New Energy Conversion and Storage, State Key Lab of Urban Water Resource and Environment, School of Chemistry and Chemical Engineering, Harbin Institute of Technology, Harbin 150001, PR China

## ARTICLE INFO

### Keywords:

Oxygen reduction reaction  
Iron and nitrogen co-doped carbon  
Hierarchical porous structure  
Dense accessible active site

## ABSTRACT

Iron and nitrogen co-doped carbon (Fe/N/C) electrocatalysts have great potential to catalyze the kinetically slow oxygen reduction reaction (ORR). Unfortunately, the ORR performance of existing Fe/N/C catalysts is seriously hindered by the insufficient density and accessibility of the atomic Fe-N<sub>x</sub> moieties. Herein, the carboxylate (OAc) molecular scissor is proposed to tailor Fe doped zeolitic-imidazolate-framework-8 (ZIF-8) at atomic scale and construct a multi-dimensional concave Fe@NC catalyst structure (Fe@MNC-OAc). This molecular scissoring strategy imparts Fe@MNC-OAc with dense accessible active sites, multidimensional mass transfer pathways, hierarchical porous structure, and entangled carbon nanotubes network. Therefore, the tailored Fe@MNC-OAc electrocatalyst exhibits excellent ORR activity in acidic media with a half-wave potential of 0.838 V, which is comparable to state-of-the-art non-precious metal catalysts. When assembled as cathode catalyst in a H<sub>2</sub>-O<sub>2</sub> proton exchange membrane fuel cell, it delivers a peak power density of 903 mW cm<sup>-2</sup>. This work provides a new approach to tailoring the catalyst architecture and improving the accessibility of active sites.

## 1. Introduction

Tremendous consumption of fossil fuels has generated a serious energy crisis and environmental degradation. The most promising approach to these issues is the development of clean and renewable energy [1–3]. Proton-exchange membrane fuel cells (PEMFCs) are widely researched as an efficient method to convert chemical energy into electrical energy via a efficient and clean way. Oxygen reduction reaction (ORR) as the core electrochemical process of PEMFC determines its overall efficiency [4–6]. Platinum group metals (PGMs) are considered state-of-the-art ORR electrocatalysts, but their scarcity and high cost hinder the large-scale applications. Hence, it is important and necessary to develop low-cost, high-activity, long-term stable PGM-free electrocatalysts to replace PGMs catalysts [7,8]. It is found that transition metal nitrogen-doped carbon has been considered one of the most promising alternatives to platinum-based catalysts [9–11]. To date, among the PGM-free catalysts studied, both theoretical and experimental results confirm that iron and nitrogen co-doped carbon electrocatalysts (Fe/N/C) exhibit the highest ORR performance [12–15]. To

obtain current density comparable to the Pt/C cathode at kinetic region under PEMFC working conditions, the loading amount of Fe/N/C electrocatalyst is about tenfold that of Pt/C, leading to a severe mass transfer limitation [16]. Therefore, the improvement of the mass activity of Fe/N/C electrocatalysts is necessary but extremely challenging.

Currently, metal-organic frameworks (MOFs) analogs, especially zinc-based zeolitic imidazolate framework (ZIF-8), are considered the most promising precursors for the preparation of M/N/C catalysts [17, 18]. However, the pyrolysis of conventional ZIF-8 precursor generally suffers from deficient porosities and mass transfer pathways leading to substantial active sites remaining inaccessible to the reactants [19–22]. Therefore, a well-designed porous architecture and promoted accessibility of active sites are critical for enhancing the performance of ZIF-8 derived catalysts. Porogenic agents such as Polyvinyl pyrrolidone (PVP) or mesoporous silica increases the specific surface area of ZIF-8-derived carbons and enriches the porous system [23,24]. However, such a synthetic strategy typically involves tedious coating, heat-treatment, and etching steps. Therefore, it is crucial to rationally design the overall morphologies and structures of the precursor to construct Fe/N/C

\* Corresponding authors.

E-mail addresses: [zyhit2022@163.com](mailto:zyhit2022@163.com) (Y. Zhang), [leizhao@hit.edu.cn](mailto:leizhao@hit.edu.cn) (L. Zhao), [shaoguangjie@ysu.edu.cn](mailto:shaoguangjie@ysu.edu.cn) (G. Shao), [wangzhib@hit.edu.cn](mailto:wangzhib@hit.edu.cn) (Z. Wang).

<https://doi.org/10.1016/j.apcatb.2022.122209>

Received 30 July 2022; Received in revised form 27 October 2022; Accepted 23 November 2022

Available online 24 November 2022

0926-3373/© 2022 Elsevier B.V. All rights reserved.

catalysts with excellent ORR performance.

In this paper, a carboxylate molecular scissor tailoring approach is proposed to design a Fe@NC catalyst with a multi-dimensional concave structure to improve the accessibility of Fe-based active sites (marked as Fe@MNC-OAc). In Fe@MNC-OAc catalysts, Fe ions exist in two different coordination environments. One is Fe-imidazole coordination form, and the other is that Fe ions bridge with unsaturated coordination surface Zn nodes through OAc molecular scissors. Therefore, the Fe content in Fe@MNC-OAc is about 1.6 times that of Fe@NC catalyst without OAc, which will cause a higher Fe<sub>Nx</sub> active site density. Furthermore, OAc enhances the porosity of Fe@NC catalysts and enables more active sites to be exposed. In acidic media, the half-wave potential ( $E_{1/2}$ ) of the Fe@MNC-OAc with optimized carboxylate dosage is 0.838 V (vs reversible hydrogen electrode (RHE)), and the stability is also significantly improved. The H<sub>2</sub>-O<sub>2</sub> PEMFC delivers a peak power density ( $P_{\max}$ ) of 903 mW cm<sup>-2</sup> when the developed Fe@MNC-OAc catalyst is applied as cathode. This shows that Fe@MNC-OAc exhibited superior electrocatalytic performance than the reported single-atom iron catalysts.

## 2. Experimental section

### 2.1. Materials

Zinc nitrate hexahydrate (Zn(NO<sub>3</sub>)<sub>2</sub>•6H<sub>2</sub>O, AR, Aladdin), 2-methylimidazole (2-MIM, 98%, Aladdin), Iron sulfate heptahydrate (FeSO<sub>4</sub>•7H<sub>2</sub>O, AR, Aladdin), Perchloric acid (HClO<sub>4</sub>, AR, Tianjin Zhengcheng Chemical Co., Ltd.), Sodium acetate anhydrous (NaOAc, AR, Tianjin BASF Chemical Co., Ltd.), Methanol (MeOH, AR, Tianjin Tianli Chemical Co., Ltd.), Isopropanol (IPA, AR, Tianjin Tianli Chemical Co., Ltd.), Nafion solution (5%, DuPont), Commercial Pt/C (20 wt%, Suzhou Sinero Technology Co., Ltd.). All reagents were directly used without further purification.

### 2.2. Preparation of Fe-doped ZIF-8 precursors with and without OAc

In a typical synthesis process, 3.20 g of 2-MIM and 2.57 g of Zn(NO<sub>3</sub>)<sub>2</sub>•6H<sub>2</sub>O were dissolved in 60 ml of MeOH, respectively, and then mixed with N<sub>2</sub> for 30 min to form a homogeneous solution. Afterward, 0.12 g FeSO<sub>4</sub>•7H<sub>2</sub>O and 0.10 g NaOAc were added to the above solution and stirred at room temperature for 24 h. Then, the solution was centrifuged, washed four times with methanol, and finally dried at 60 °C for overnight. The as-prepared product was denoted as Fe@ZIF8-OAc. Control samples of Fe-doped ZIF-8 precursor with Fe but without OAc were prepared similarly, which were labelled as Fe@ZIF8.

### 2.3. Preparation of Fe/N/C catalysts with and without OAc

The catalysts were prepared by a simple one-step pyrolysis of Fe@ZIF8-OAc or Fe@ZIF8 precursors under Ar atmosphere at 900 °C. The following temperature programming was used: the temperature was firstly increased from room temperature to 900 °C at a rate of 5 °C min<sup>-1</sup>, and held at 900 °C for 3 h, finally cooled to room temperature naturally. Next, acid leaching treatment in 0.5 M H<sub>2</sub>SO<sub>4</sub> solution at 80 °C for 5 h was carried out to remove Fe NPs and open porous structures of samples. Typically, 100 ml acid solution was used for 100 mg sample. An additional heat treatment at 700 °C under N<sub>2</sub> flow for 1 h is necessary to repair the carbon structure. The corresponding products were labelled as Fe@MNC-OAc and Fe@NC.

### 2.4. Preparation of Fe@MNC-xOAc (x = 0.05, 0.2, 0.3) catalysts

To investigate the effect of the doping amount of OAc on the properties and performance of the catalyst, several other catalysts were prepared at OAc contents of 0.05 g, 0.2 g and 0.3 g were prepared for comparison with the doping amount of 0.1 g.

### 2.5. Physicochemical characterizations

The powder X-ray diffraction (XRD) spectra was obtained by a D2 PHASER XE-T diffractometer (Bruker Corporation) with a Cu K $\alpha$  X-ray source operating at 30 kV and 10 mA, scanning at a rate of 6° min<sup>-1</sup>. The standard CIF file of ZIF-8 is downloaded from Cambridge Crystallographic Data Centre (CCDC) website and the XRD spectrum is simulated by Mercury software. X-ray photoelectron spectroscopy (XPS) was recorded on a Thermo Scientific K-Alpha (Thermo Fisher Scientific) and XPSPEAK41 software was used for data analysis. Monochromatic X-rays were generated by an Al K $\alpha$  source (1486.7 eV), and all binding energies were calibrated by the peak position of C 1s peak (284.8 eV). Raman spectra measurements were performed on an in Via-Reflex confocal Raman microscope (inVia-Reflex, Renishaw Instruments), excited with a 532 nm laser. The content of metal elements in the catalyst was tested by a machine ICP-OES Agilent 5110 (Agilent Technologies). Specific surface area and porosity properties were performed using a Surface Area Porosity Analyzer (BSD-PS, BeiShiDe Instrument) at 77 K, degassed at 150 °C before measurement. The specific surface area were determined by Brunauer-Emmett-Teller (BET) method. The surface morphologies were observed on a field emission scanning electron microscopy (SEM) Merlin Compact (Carl Zeiss AG). High resolution transmission electron microscopy (HRTEM), High-angle annular dark-field-scanning transmission electron microscope (HAADF-STEM) and STEM energy dispersive X-ray spectroscopy (STEM-EDS) images were obtained using Tecnai G2 F20 TEM (Thermo Fisher Scientific). Aberration-corrected HAADF-STEM (AC-HAADF-STEM) images were acquired with Themis G2 300 (FEI Company). The X-ray absorption spectroscopy (XAS) of Fe K edge absorbance was performed at beamline BL14W1 of the Shanghai Synchrotron Radiation Facility (SSRF), with a storage ring energy of 3.5 GeV. An open-source XAS data analysis system (Demeter) was used to calibrate (Athena module) XANES and curve fitting (Artemis module) EXAFS. Wavelet analysis was performed using HAMA software developed by Marina Chukalina and Harald Funke. The XAFS raw data were processed with background-subtraction, normalization and Fourier transformation by the standard procedures with Athena module of the IFEFFIT software packages.

### 2.6. Electrochemical measurements

The electrochemical performance was measured by electrochemical workstation chi760e (CH Instruments Ins.) with a three electrode system, in which reversible hydrogen electrode (RHE) and platinum wire were used as the reference and counter electrodes, respectively. A rotating ring-disk electrode (RRDE) with a glassy carbon disk (5.6 mm in diameter) and a Pt ring were used as the working electrode. When not specially stated, the acidic electrolytes were 0.1 M HClO<sub>4</sub>. To prepare the working electrode, the catalyst ink for the RRDE tests was prepared by ultrasonically dispersing 5.0 mg catalysts and 30  $\mu$ l Nafion solution (5 wt%) into 2.0 ml isopropanol solution. The ink was drop-casted on the disk electrode with a controlled loading of 0.8 mg cm<sup>-2</sup> and dried at room temperature to yield a thin-film electrode.

Cyclic voltammetry (CV) tests were carried in O<sub>2</sub>/N<sub>2</sub>-saturated electrolyte with a scan rate of 5–50 mV s<sup>-1</sup>. The electrocatalytic activity for ORR was tested by staircase voltammetry (SCV) from high potential to low potential with the step of 0.05 V at intervals of 30 s in O<sub>2</sub>-saturated electrolyte and a rotation rate of 900 rpm. Electrochemical impedance spectroscopy (EIS) was measured at a potential of 0.6 V (all potentials in this paper are referenced to RHE). Accelerated durability test (ADT) were scanned between 0.6 and 1.1 V with a scan rate of 100 mV s<sup>-1</sup>. Moreover, the kinetic current density  $J_k$  was calculated from the Koutecky-Levich Eq. (1). the yielding of H<sub>2</sub>O<sub>2</sub> intermediate (H<sub>2</sub>O<sub>2%</sub>) and electron transfer number ( $n$ ) were calculated from Eqs. (2) and (3).

$$\frac{1}{J} = \frac{1}{J_k} + \frac{1}{J_d} \quad (1)$$

$$H_2O_2\% = 200 \times \frac{I_r}{N \times I_d + I_r} \quad (2)$$

$$n = 4 \times \frac{N \times I_d}{N \times I_d + I_r} \quad (3)$$

In the first equation,  $J$  is the measured current density,  $J_k$  and  $J_d$  represent the kinetic and diffusion-limiting current density. In the next two equations,  $I_r$  and  $I_d$  represent the current on the disk and the ring of RRDE, and  $N$  is the current collection efficiency of the Pt ring ( $N = 0.37$ ).

The electrochemical double-layer capacitance ( $C_{dl}$ ) of the carbon-based material was determined from double layer charging curves in non-faradic potential range of 0.50–0.65 V (vs. RHE). The electrochemically active surface area (ECSA) was further calculated based on:

$$ECSA(m^2g^{-1}) = \frac{C_{dl}}{C_{GDE} \times L_{cata}}$$

where  $C_{GDL}$  is the double layer capacitance of GCE ( $0.02 \text{ mF cm}^{-2}$ ) [25] and  $L_{cata}$  is the catalyst loading amount ( $8.0 \text{ g m}^{-2}$ ).

## 2.7. Quantification of the accessible active sites

The accessible site densities of  $FeN_4$  sites in the Fe@NC and Fe@MNC-OAc were determined according to the method described by Kucernak et al. [20]. The method is based on the adsorption and reduction of nitrite ( $NO_2^-$ ) on the central Fe atoms of  $FeN_4$  sites.

The accessible site density (SD) and intrinsic turnover frequency (TOF) were calculated using the following equations [20,26]:

$$SD(mol\text{g}^{-1}) = \frac{Q_{strip}(Cg^{-1})}{n_{strip}F(Cmol^{-1})}$$

$$TOF(s^{-1}) = \frac{n_{strip}j_k(mAcm^{-2})}{Q_{strip}(Cg^{-1})L_C(mgcm^{-2})}$$

where  $Q_{strip}$  is the excess coulometric charge associated with the stripping peak,  $F$  is the Faraday constant,  $n_{strip}$  is the number of electrons associated with the reduction of one nitrite per site ( $n_{strip} = 5$ ),  $j_k$  is the kinetic current density at 0.8 V,  $L_C$  is the catalyst loading during the reversible nitrite poisoning experiments ( $0.80 \text{ mg cm}^{-2}$ ).

## 2.8. Fuel cell tests

The homemade catalyst was mixed with perfluorosulfonic acid ionomer (Nafion D520) (56.5% ionomer content in the mixture) and then sonicated in isopropanol and deionized water (in the volume ratio of 4:1) to prepare a slurry with solid content of 2.5% (catalyst and dry ionomer). The membrane electrode (MEA) was prepared by the CCM (Catalyst Coating Membrane) method using ultrasonic spraying equipment, and the above dispersed slurry was uniformly deposited on a proton exchange membrane (Nafion NC700) to a catalyst loading of  $3.0 \text{ mg cm}^{-2}$ . Then the gas diffusion layer (AvCarb GDL MB30) was placed on the catalyst layer as the cathode side of MEA.

Commercial 20% Pt/C (SPT-20, CAS NO. 7440–06–4) was mixed with Nafion D520 (44.4% ionomer content in the mixture) and then sonicated and dispersed in isopropanol and deionized water (in the volume ratio of 1:1) to prepare a slurry with solid content of 1.0% (catalyst and dry ionomer). After the same treatment, the catalyst loading of  $0.1 \text{ mg}_{Pt} \text{ cm}^{-2}$  and a commercial gas diffusion layer was uniformly placed on the anode side. The active area of the MEA prepared above was  $5 \text{ cm}^2$ . For comparison with the noble metal catalyst (Pt/C) and to evaluate the practicality of the homemade catalyst, the same slurry formulation was used to prepare the noble metal MEA with a cathode loading of  $0.3 \text{ mg}_{Pt} \text{ cm}^{-2}$  and an anode loading of  $0.1 \text{ mg}_{Pt} \text{ cm}^{-2}$ .

In this paper, MEA testing was performed using the Scribner 850e fuel cell test system. After sufficient activation, the open-circuit voltage was first observed at  $80^\circ\text{C}$  and 100% RH test conditions, followed by the measurement of the  $H_2(500 \text{ sc.c.m.})-O_2(500 \text{ sc.c.m.})/\text{Air}(1000 \text{ sc.c.m.})$  polarization (I-V) versus power density (I-P) curves from the open-circuit voltage to 0.2 V. The variation of polarization current density versus power density in the curve was observed at the test back pressure of 100 kPa. In addition, the electrochemical impedance spectrum of a single cell was tested at a constant cell voltage of 0.6 V and other conditions, with a frequency range of  $10^{-1}$  to  $10^5 \text{ Hz}$  and a cross-frequency amplitude of 10 mV, and the spectrum was analyzed by Zview software.

## 3. Results and discussion

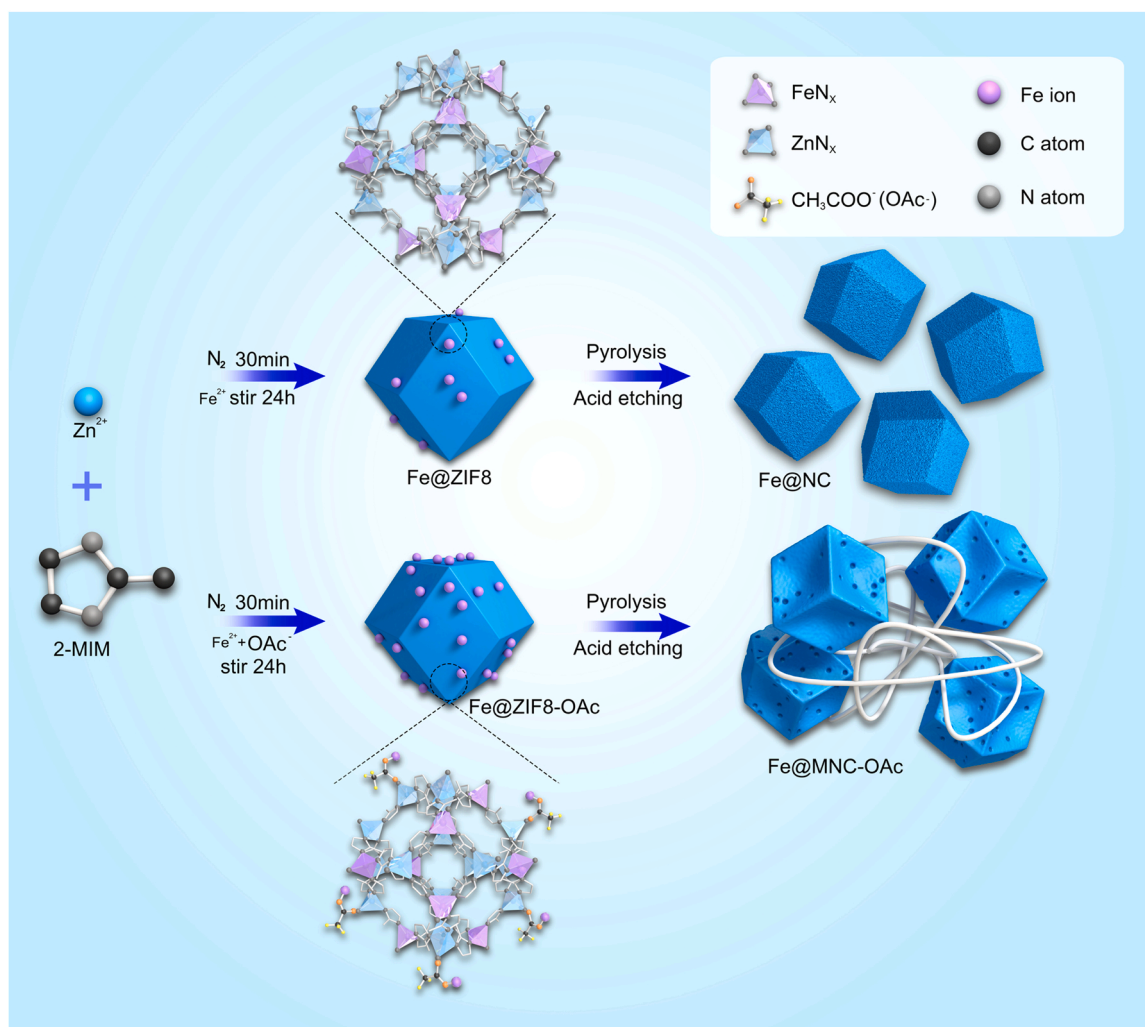
### 3.1. Synthesis and physical characterizations

As indicated in Scheme 1, accompanying the Fe-doping, OAc function as molecular scissors was introduced into the ZIF8 precursor. Simply, with the addition of a mixture of  $FeSO_4 \cdot 7H_2O$  and NaOAc to the suspension of ZIF-8 particles for 24 h, Fe and OAc ions were introduced into the ZIF8 particles. After centrifugation and vacuum drying, the Fe-doped ZIF-8 precursors containing OAc (denoted as Fe@ZIF8-OAc) were collected. A Fe@ZIF8 precursor control without OAc was prepared. It has been reported that there is mutual coordination between carboxylate groups and metal ions [27]. Scheme 1 also shows the Fe doping mechanism of ZIF-8 particles in the presence and absence of OAc. When OAc is present, Fe ions are doped with unsaturated coordination surface Zn nodes via OAc, while in the absence of OAc, Fe ions are doped into the Fe-imidazole coordination.

#### 3.1.1. Characterization of morphology and structure

The scanning electron microscope (SEM) and transmission electron microscope (TEM) have clearly demonstrate an effect of OAc addition on the morphology and structure for the samples. As expected, a dodecahedral shape with a smooth surface can be obtained by direct pyrolysis of the Fe@ZIF8 precursor without OAc (Fig. 1a,b). The Fe@MNC-OAc catalysts shows a multidimensional concave structure assembled by 3D concave dodecahedra and 1D fluffy entangled carbon nanotubes (CNTs) (Fig. 1c-e). Besides, a closer inspection of the Fe@MNC-OAc revealed that the carbonized substrates were amorphous C, and no crystal Fe or Fe compounds were found, as shown in the high-resolution TEM (HR-TEM) image (Fig. 1f) and the selected area electron diffraction (SAED) analysis (inset in Fig. 1f). To examine the Fe dispersion in the samples, aberration-corrected HAADF-STEM images measurements were carried out (Fig. 1g). It can be clearly observed that the high density of single iron atoms in Fe@MNC-OAc is uniformly distributed in the porous carbon substrate, which makes it possible for forming an atomically dispersed  $Fe-N_x$  fraction. It should be noted that several small Fe clusters were also detected as the slightly aggregated of Fe atoms, which was not identified by TEM. In combination with high-angle annular dark-field scanning transmission electron microscopy (HAADF-STEM) and EDS elemental mappings, larger Fe nanoparticles (NPs) (Fig. 1h) are not observed in Fe@MNC-OAc, and the the results of the corresponding elemental mapping show uniform distribution of C, N, and Fe atoms for the framework (Fig. 1i). Another phenomenon that needs to be revealed is the relationship between OAc doping and the appearance of carbon nanotubes. The formation of CNTs accompanies the appearance of Fe clusters, inferring that the Fe clusters catalyzed carbon nanotubes formation [28]. The doping of OAc increases the Fe content of the catalyst (Fig. S2), and the sufficient Fe content ensures the formation of carbon nanotubes.

Obviously, the presence of OAc greatly influences the morphology, porosity, and Fe content of the synthesized catalysts. Inductively coupled plasma optical emission spectrometry (ICP-OES) indicates that Fe content of Fe@MNC-xOAc ( $x = 0.05, 0.1, 0.2, 0.3$ ) catalyst is higher than Fe@NC samples (Fig. S2), and the Fe content is highest at 0.1 g of



**Scheme 1.** The synthesis diagram of Fe@NC and Fe@MNC-OAc.

OAc doping. During Fe@ZIF8 pyrolysis, imidazole is converted to N-doped porous carbon and Zn species evaporate to form nanostructures with atomically dispersed FeN<sub>4</sub> coordination. For Fe@MNC-OAc samples, previous DFT calculations indicated that due to strong interaction of Fe ions with carboxylates, it is difficult for Zn ions to be directly replaced by Fe ions coordinated with carboxylates [29], so Fe ions act as the linker is more likely to be doped by OAc. X-ray diffraction (XRD) spectra of samples showed two broad diffraction peaks, which correspond to the (002) and (101) planes of graphitized carbon at 24.3° and 43.7°, respectively (Fig. S4b) [30]. No significant peaks related to Fe-containing compounds were recognized for all samples, confirming the monoatomic state of Fe, that could be attributed to highly dispersed Fe atoms within the skeleton. Notably, the Fe clusters in Fe@MNC-OAc do not display any peaks due to their small size and low content. The degree of defects in Fe@NC and Fe@MNC-OAc was investigated using Raman spectra. The peak at 1350 cm<sup>-1</sup> corresponds to the D-band, revealing the structural defects of carbon, and G-band (1580 cm<sup>-1</sup>) indicates the presence of the graphitic structure in carbon materials. The wider D-band of Fe@MNC-OAc catalyst indicates that the introduction of OAc enhances the degree of defects. With Fe@NC and Fe@MNC-OAc catalysts, the area ratios for the D and G bands (Area<sub>D</sub>/Area<sub>G</sub>) are 1.48 and 1.81, respectively (Fig. 2b and Fig. S3). The Area<sub>D</sub>/Area<sub>G</sub> value for the Fe@MNC-OAc material is much higher than the other catalysts, demonstrating an increase in the degree of defects.

Both surface area and porous structure of the samples are further studied through N<sub>2</sub> adsorption-desorption isotherms. The Fe@MNC-OAc

shows higher BET surface area compared to the prepared Fe@NC catalyst ( $S = 600.28 \text{ m}^2 \text{ g}^{-1}$ ) (Fig. 2c). In comparison, the prepared Fe@MNC-OAc catalyst has the highest BET surface area ( $1181.687 \text{ m}^2 \text{ g}^{-1}$ ), including a microporous surface area of  $798.663 \text{ m}^2 \text{ g}^{-1}$  and an external surface area of  $383.024 \text{ m}^2 \text{ g}^{-1}$  (Fig. S6 and Table S2). The Fe@MNC-OAc and Fe@NC catalysts are both characterised by a typical type IV isotherm with the significant hysteresis loop ( $0.45 < P/P_0 < 0.9$ ), which is typical of mesoporous and micropore coexisting structures. However, the Fe@MNC-OAc catalyst has a higher porosity (Table S2). The pore size distribution of the samples is obtained through the BJH method. The co-existence of micropores and mesopores indicated that hierarchical porous structures are formed in the Fe@MNC-OAc catalyst with pore sizes ranging from 0.4 to 15 nm. To elucidate the impacts of OAc on the pore structure of catalysts, compared the pore structures of these catalysts (Fig. 2d and Fig. S5), and it is found that OAc led to an increase in both micropores and small size mesopores. This result indicates that the carbon matrix is subjected to oxidative corrosion of OAc during high temperature pyrolysis, which increases the number of micropores. That oxidative corrosion of OAc leads to the loss of some pore walls thus allowing partial consolidation of micropores into mesopores [31]. These results suggest that the carboxylate molecular scissor tailoring method is effective in converting ZIF-derived microporous structures into hierarchically porous structures, which increases the density of active sites and promote electrocatalytic electron transfer.

XPS survey spectrum (Fig. S7) affirms the presence of C, N, O and Fe



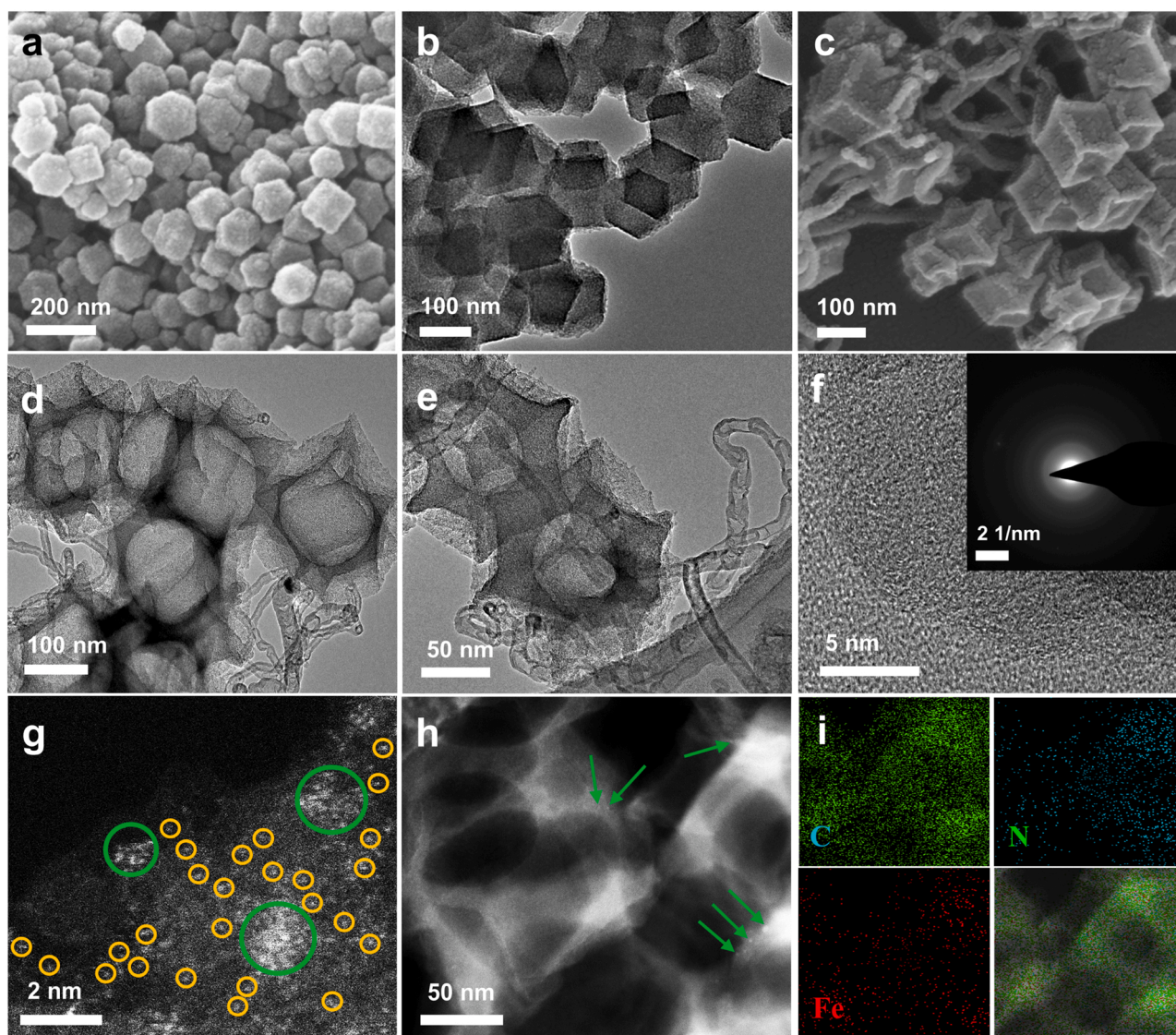


**Fig. 1.** a) SEM image for Fe@NC; b) TEM image for Fe@NC; c) SEM image for Fe@MNC-OAc; d) and e) TEM images for Fe@MNC-OAc; f) HR-TEM image for the Fe@MNC-OAc (the inset in Fig. 1g indicates its associated SAED pattern); g) AC HAADF-STEM image showing Fe clusters (green circles) and its satellite Fe atoms (yellow circles); h) HAADF-STEM image of Fe@MNC-OAc (The bright dots marked by the green arrows represent Fe clusters.); i) its related C, N, and Fe elements distribution for Fe@MNC-OAc.

elements of the samples, which is consistent with the results of the elemental mapping. For an in-depth study on the chemical state of N and Fe, high-resolution C 1s and high-resolution N 1s spectra for these samples were deconvoluted [32]. The high-resolution N 1s spectrum of Fe@MNC-OAc is deconvolution to five types of N species, which corresponded to pyridine nitrogen (397.7 eV), Fe-N<sub>x</sub> (398.6 eV), pyrrole nitrogen (399.2 eV), graphite nitrogen (400.6 eV) and oxidized nitrogen (403.6 eV) (Fig. 3a) [33]. Similarly, these peaks are identified in Fe@NC. The Fe-N peak confirms that the Fe species are uniformly anchored into the framework as Fe-N<sub>x</sub> structures. The pyridine nitrogen species are considered the main active site and supply anchoring sites for Fe single atoms. It is observed that Fe-N species in the Fe@MNC-OAc catalyst shifts to higher binding energy compared to the Fe@NC (398.1 eV). It indicates that the electronic configuration of Fe-N species can be changed after the introduction of Fe clusters. Relative contents of various N species are evaluated from the XPS data (Fig. S9) [34]. The content of pyridine N and graphite N is higher for Fe@MNC-OAc. Pyridine N can increase the current density with graphite N accelerating the 4e<sup>-</sup> transport path, which improves the ORR performance. The C 1s spectra of Fe@MNC-OAc is deconvolution into five peaks (Fig. 3b), C-C

(284.4 eV), C-N (284.8 eV), C-O (285.7 eV), C=C (286.6 eV) and O-C=O (289.7 eV) [35]. In comparison with Fe@NC (285.1 eV), the C-N peak in Fe@MNC-OAc shifts to a lower binding energy. The change in binding energy indicates the electron redistribution followed by electron transfer to the carbon substrate. The Fe 2p XPS spectra displays typical four peaks that are attributed to the Fe<sup>2+</sup> and Fe<sup>3+</sup> contributions of Fe-N<sub>x</sub> (Fig. S8). The presence of Fe<sup>0</sup> indicates the appearance of ultra-small cluster of iron atoms in this catalyst [36].

### 3.1.2. Characterization of active site structure

The Fe atom coordination environment and chemical state in the Fe@MNC-OAc are studied using hard X-ray absorption spectroscopies (XAS). Fe K-edge X-ray absorption near edge structure (XANES) is applied to study the oxidation state for Fe atoms (Fig. 3c). The XANES of Fe@MNC-OAc exhibits a higher absorption edge than Fe foil and lower than FePc, showing that Fe has an oxidation state between 0 and +2 [37,38]. Since Fe@MNC-OAc is expected to contain FeN<sub>4</sub> active sites, iron phthalocyanine (FePc) was considered a reference for Fe-N scattering paths. In the Fourier-transformed (FT) extended X-ray absorption fine structure (EXAFS) spectra of Fe@MNC-OAc shows peaks at about

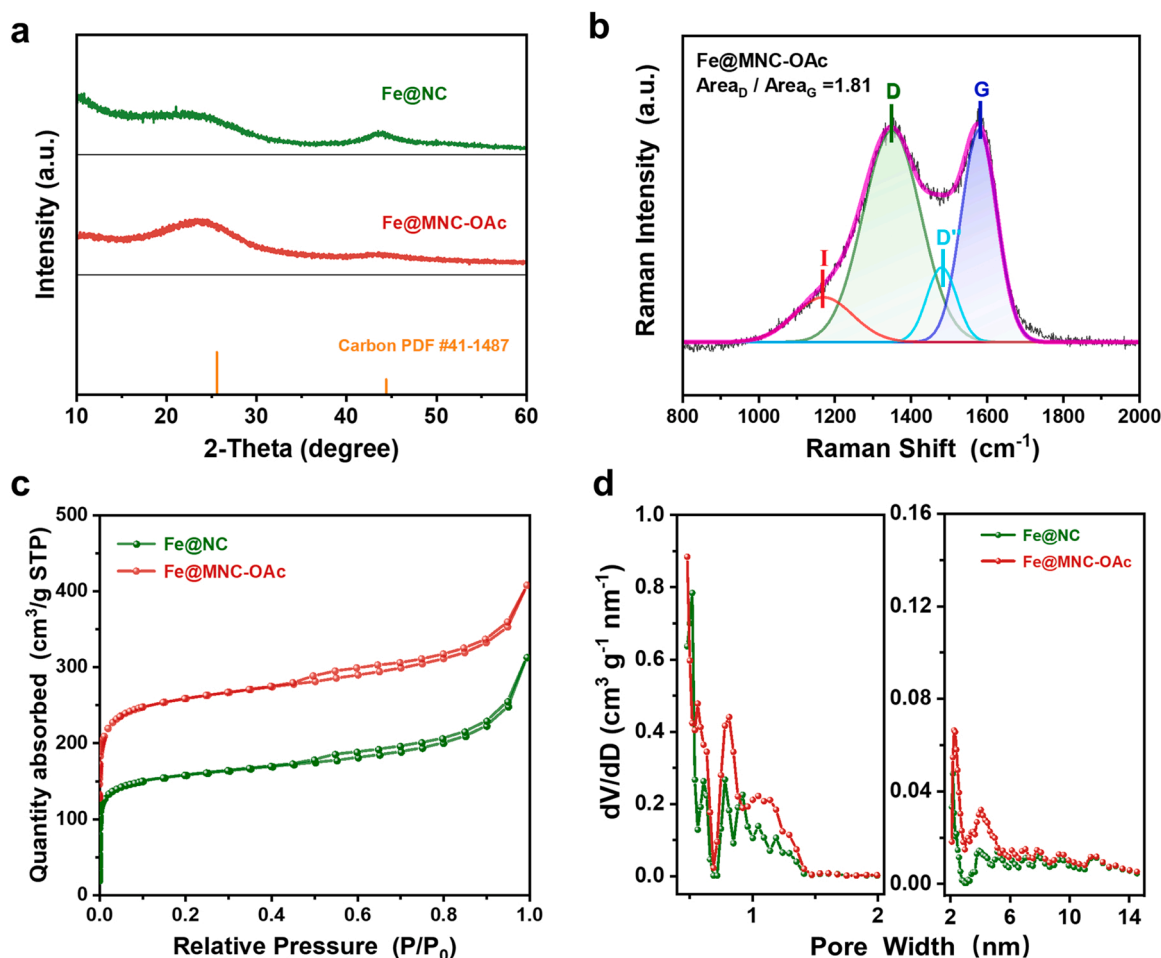


Fig. 2. a) XRD patterns of Fe@NC and Fe@MNC-OAc; b) Raman spectra of Fe@MNC-OAc; c)  $N_2$  adsorption-desorption results; d) the results of the pore size distribution of the Fe@NC and Fe@MNC-OAc.

1.5 Å and 2.0 Å, which corresponds to Fe-N and Fe-Fe bonds (Fig. 3d) [39,40]. In conclusion, the above confirms the co-existence of iron atoms in the form of mononuclear and multinuclear centers. The slightly different R values compared to Fe-Fe bonds of Fe foil (2.2 Å) may be due to the different degrees of coordination between bulk Fe and Fe clusters [41,42]. Then, the data are fitted and a fit with a Fe-N coordination number of about four is obtained (Fig. S10 and Table S3). Meanwhile, the Fe-Fe coordination numbers (CN) is 1.47, which further indicates the presence of clusters for the sample. Since the Fourier transform is based on the coordination distance to determine the coordination atoms, it is difficult to distinguish atoms with close coordination distances. In addition, the wavelet transform (WT) EXAFS can resolve both the K and dependence of the absorption signal [43,44]. The  $k^3$ -weighted WT EXAFS spectra of FePc and Fe foil show contour intensity maxima at  $5.5 \text{ Å}^{-1}$  and  $8 \text{ Å}^{-1}$  (Fig. 3e). The maxima of the Fe@MNC-OAc sample  $k$  are very close to those determined of FePc ( $5.5 \text{ Å}^{-1}$ ), illustrating similar Fe-N<sub>4</sub> coordination with FePc. In addition, an extra peak occurs at high  $k$  values ( $\approx 8 \text{ Å}^{-1}$ ), which may be attributed to Fe-Fe scattering.

### 3.2. Catalyst activity for ORR

ORR performance of the obtain Fe@MNC-OAc sample is investigated because of its unique multidimensional concave structure, graded porosity and high surface area. Fig. S20 shows that no visible redox peaks are detected in the  $N_2$ -saturated solution. On the contrary, at  $O_2$  saturation, all catalysts exhibit visible redox peaks, indicating the presence of an effective ORR process. Fe@MNC-OAc exhibit the more

positive ORR peak (0.79 V) than the other comparison samples. The ORR electrochemical performance of the samples is further evaluated through staircase voltammetry (SCV) in an electrolyte containing 0.1 M  $HClO_4$  on a rotating ring-disk electrode (RRDE). In Fig. 4a, the ORR onset potential ( $E_{onset}$ ) of Fe@MNC-OAc is 0.96 V. The half-wave potential ( $E_{1/2} = 0.838 \text{ V}$ ) and kinetic current density ( $J_k @ 0.8 \text{ V} = 15.87 \text{ mA cm}^{-2}$ ) at 0.8 V for Fe@MNC-OAc are considerably better than other comparison samples and close to the commercial Pt/C (20 wt%) catalysts ( $E_{1/2} = 0.862 \text{ V}$ ,  $J_k @ 0.8 \text{ V} = 18.25 \text{ mA cm}^{-2}$ ) (Fig. S11a and Fig. S12). Notably, the  $E_{1/2}$  and  $J_k @ 0.8 \text{ V}$  of Fe@MNC-OAc exceed majority of the recently reported iron-based catalysts (Table S4). The smaller Tafel slope of  $70.4 \text{ mV dec}^{-1}$  compared to other comparison samples and commercial Pt/C (20 wt%) is further evidence the favorable ORR kinetic process of Fe@MNC-OAc (Fig. 4b).

### 3.3. Mechanism of catalyst performance enhancement for ORR

The higher BET surface area of Fe@MNC-OAc facilitate exposed more active sites, thus enhancing the oxygen reduction activity. The presence of one-dimensional CNTs, except for the nature of high-density active centers and porous structures, can enhance the ORR activity of electrocatalysts [45]. One-dimensional CNTs were shown to have exhibited remarkable charge extraction capability in electrochemical reactions. The multi-dimensional structure comprised of ZIF8 and CNTs can further facilitate ORR activities through covalent C-C bonds based on  $\pi$ - $\pi$  stacking [46,47]. In contrast, the multi-dimensional structure with an interconnected frameworks has a larger specific area.



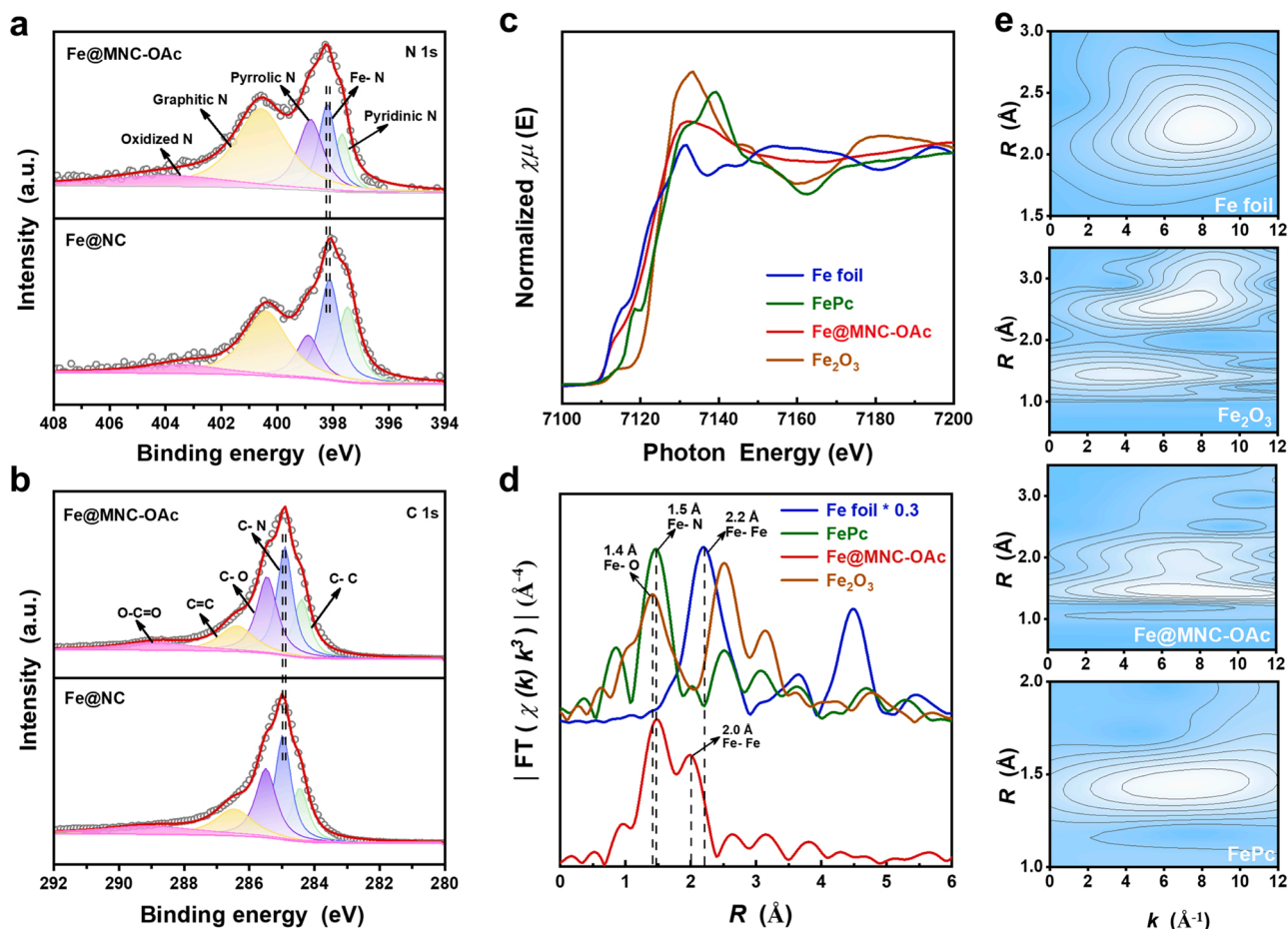


**Fig. 3.** a) High-resolution XPS spectra for N 1s; b) High-resolution XPS spectra for C 1s; c) Normalized Fe K-edge XANES spectra for Fe@MNC-OAc, Fe foil, FePc and Fe<sub>2</sub>O<sub>3</sub>; d)  $k^3$ -weighted Fourier transformed EXAFS spectra at R space of Fe@MNC-OAc, Fe foil, FePc and Fe<sub>2</sub>O<sub>3</sub>; e)  $k^3$ -weighted wavelet transformed Fe K edge EXAFS spectra of Fe@MNC-OAc, Fe foil, FePc and Fe<sub>2</sub>O<sub>3</sub>.

Furthermore, the multi-dimensional structure will form more channels to promote the transfer rate of electrons or reactants, further enhancing the rate of the electrocatalytic reaction. In situ electrochemical nitrite poisoning experiments are performed to determine the SD and TOF of the FeN<sub>4</sub> sites of samples (Fig. 4f and Fig. S21) [20,48]. The accessible FeN<sub>4</sub> active site density in Fe@MNC-OAc was identified to be 34.17  $\mu\text{mol g}^{-1}$ , with a higher level than that of Fe@NC at 23.56  $\mu\text{mol g}^{-1}$ . As a result, the intrinsic TOF (calculated from the accessibility) of Fe@MNC-OAc is up to 4.8 s<sup>-1</sup> at 0.8 V, which is 1.5 times higher than 3.1 s<sup>-1</sup> for Fe@NC (Fig. 4f) and exceeds those reported for Fe-N-C electrocatalysts (Table S7).

In addition, the coexistence of atoms M-N-C and metal clusters extends the M-N bond, thus changing the M-N-C coordination environment and facilitating the four-electron transfer pathway [33]. To investigate the ORR pathway over different catalysts, the RRDE experiment is performed to detect the H<sub>2</sub>O<sub>2</sub> Formation. In the potential range of 0.1–0.8 V, the H<sub>2</sub>O<sub>2</sub> yield of Fe@MNC-OAc is below 1.0%, which is obviously superior to the comparison sample (Fig. 4c). This result indicates a high selectivity of Fe@MNC-OAc for the four-electron reaction process to generate H<sub>2</sub>O ( $\text{O}_2 + 4\text{H}^+ + 4\text{e}^- \rightarrow 2\text{H}_2\text{O}$ ) with an electron transfer number of about 3.99. Thus, the catalyst exhibits a promising ORR kinetic process and high selectivity for the four-electron reaction process. Electrochemically active surface area (ECSA) of the catalysts are investigated through assessing the double layer capacitance ( $C_{\text{dl}}$ ) calculated from the CV curves of the non-Faraday region [49]. As shown Fig. S14, the  $C_{\text{dl}}$  value of 132.6 mF cm<sup>-2</sup> for the Fe@MNC-OAc catalyst is higher than all other comparison samples, indicating a higher ECSA for Fe@MNC-OAc. Moreover, ECSA of Fe@MNC-0.1OAc is calculated to be

414.3 m<sup>2</sup> g<sup>-1</sup>, which is higher than Fe@NC(292.5 m<sup>2</sup> g<sup>-1</sup>), in agreement with the analysis of BET. The mass activity of Fe@MNC-OAc is determined to be 19.84 A g<sup>-1</sup> at 0.8 V, much higher than 7.05 A g<sup>-1</sup> for Fe@NC (Fig. S18).

### 3.4. Stability of the catalyst for ORR

The stability of Fe@MNC-OAc and commercial Pt/C (20 wt%) was assessed by chronoamperometry for 15,000 s at 900 rpm in O<sub>2</sub>-saturated 0.1 M HClO<sub>4</sub> electrolyte. Fe@MNC-OAc retains up to 96.27% with the original current density (Fig. 4d), outperforming the Pt/C (20 wt%) catalyst (which retained about 30%), showing its excellent stability. The excellent stability of the Fe@MNC-OAc was further confirmed by continuous CV tests at a potential range of 0.6–1.0 V at 50 mV s<sup>-1</sup> in O<sub>2</sub>-saturated acidic conditions. After 5000 potential cycles between 0.6 and 1.0 V in an O<sub>2</sub>-purged 0.1 M HClO<sub>4</sub> at ambient temperature, Fe@MNC-OAc exhibits the best stability with an E<sub>1/2</sub> loss of only 5 mV, much smaller than those of Fe@NC (9 mV) and Pt/C (13 mV) (Fig. 4e). Besides, the almost identical cyclic voltammetry curves during the stability tests (inset of Fig. 4e) indicate excellent resistance to carbon corrosion. Moreover, the E<sub>1/2</sub> of Fe@MNC-OAc catalyst decreased only 9 mV after 10,000 cycles (Fig. S17). In addition, negligible current attenuation in Fe@MNC-OAc is observed after adding 3 ml methanol to the electrolyte, indicating excellent methanol tolerance (Fig. S20c). The CO tolerance test further demonstrates that the Fe catalyst has excellent resistance to CO poisoning (Fig. S22). The morphology of this catalyst are observed after stability testing. The SEM images shows that multidimensional concave architecture of Fe@MNC-OAc is well preserved without

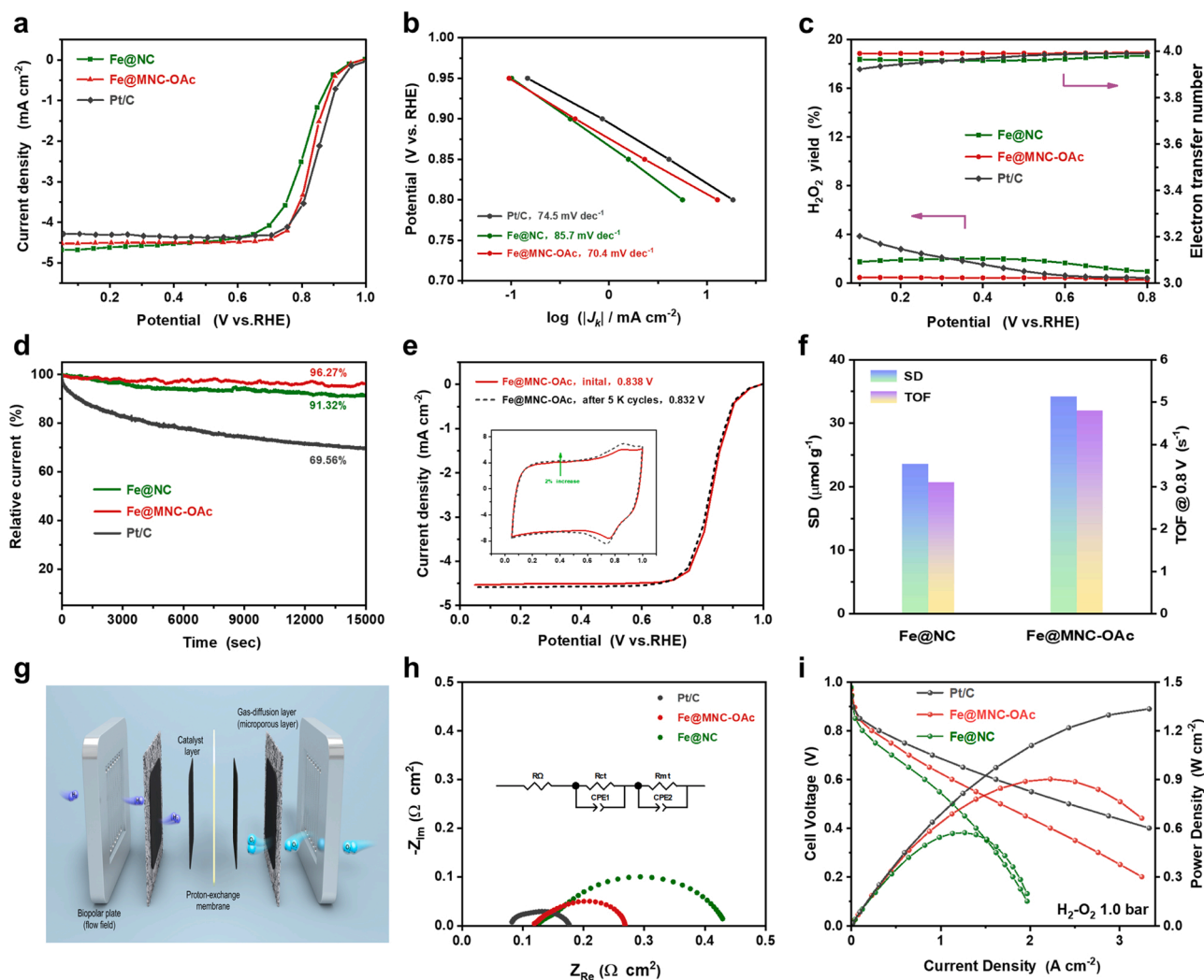


**Fig. 4.** a) SCV tests of these samples on RDE saturated with O<sub>2</sub> at 0.1 M HClO<sub>4</sub> (900 rpm); b) Tafel slope for the samples; c) The H<sub>2</sub>O<sub>2</sub> yields and electron transfer numbers of Fe@NC, Fe@MNC-OAc and Pt/C; d) Chronoamperometric responses of the Fe@NC, Fe@MNC-OAc and Pt/C at 0.75 V in O<sub>2</sub>-saturated 0.1 M HClO<sub>4</sub> (900 rpm); e) ORR polarization curves of Fe@MNC-OAc before and after 5000 cycles (0.6–1.0 V vs. RHE) in O<sub>2</sub>-saturated 0.1 M HClO<sub>4</sub>; f) SD and TOF of Fe-N<sub>4</sub> sites of Fe@NC and Fe@MNC-OAc electrocatalysts; g) Schematic diagram of PEMFC; h) Nyquist plots of Fe@NC, Fe@MNC-OAc and Pt/C at 0.6 V; i) Polarization and power density curves of 1.0 bar H<sub>2</sub>-O<sub>2</sub> PEMFC using Fe@NC, Fe@MNC-OAc and Pt/C as cathode materials.

obvious structural changes. In contrast, the dodecahedral structure of Fe@NC shows significant agglomeration and collapse, further verifying the good durability of the Fe@MNC-OAc catalyst (Fig. S19).

### 3.5. Fuel cell tests performance evaluation

Since the Fe@MNC-OAc exhibited superior ORR activity, PEMFC performance is tested using it as cathode catalyst. The loading of Fe@MNC-OAc catalyst at the cathode is reduced to 0.0765 mg<sub>Fe</sub> cm<sup>-2</sup> due to its high ORR mass activity. In the H<sub>2</sub>-O<sub>2</sub> system at 1.0 bar, the Fe@MNC-OAc electrocatalyst shows high P<sub>max</sub> of 903 mW cm<sup>-2</sup>, while the measured value for the Fe@NC electrocatalyst is 565 mW cm<sup>-2</sup> (Fig. 4i). Simultaneously, Fe@MNC-OAc has a P<sub>max</sub> of 415 mW cm<sup>-2</sup> under 1.0 bar H<sub>2</sub>-air condition (Fig. S23). Under PEMFC experimental conditions, the P<sub>max</sub> value obtained for Fe@MNC-OAc is one of the higher values for the M@NC ORR catalyst (Table S8). To measure the mass transfer resistance (R<sub>mt</sub>) and charge transfer resistance (R<sub>ct</sub>) for the MEA prepared from the catalyst, the Nyquist plots of EIS was measured with the potential of 0.6 V and simulated with Zview (Fig. 4h) [50]. However, both R<sub>ct</sub> and R<sub>mt</sub> of MEA prepared from Fe@MNC-OAc are much smaller than those of MEA prepared from Fe@NC but slightly larger than commercial Pt/C (Table S5). The EIS results demonstrate

that Fe@MNC-OAc has higher activity than Fe@NC.

High density of available active sites for Fe@MNC-OAc catalyst ensures high kinetic activity of the cathode; abundant 1D carbon nanotubes in it also accelerates the electron transport and reduces the internal resistance of the whole cell. Moreover, the low loading cathode catalyst loading ensures the mass transfer to the cathode. However, Fe@MNC-OAc is still lower than Pt/C cathode (1334 mW cm<sup>-2</sup>), the stability of Fe@MNC-OAc electrocatalyst is still deficient. Additional work should be done to enhance the electrochemical properties of Fe@NC catalysts. The introduction of OAc molecular scissors prepared a catalyst with a hierarchical porous structure. The abundant specific surface area and the pore structure significantly increased the accessible FeN<sub>4</sub> active sites. As a result, the obtained Fe@MNC-OAc contains a high density of accessible single atom FeN<sub>4</sub> active sites and exhibits greatly enhanced ORR activity compared with reported other Fe/N/C and catalysts. Moreover, the Fe single atom is the main active sites and there are interactions between the Fe clusters and FeN<sub>4</sub>. Our strategy will help develop high-performance, cost-effective M/N/C ORR catalysts, especially MOFs-based catalytic materials.



## 4. Conclusions

In summary, a unique carboxylate-molecular scissor tailoring method is developed to prepare the Fe@MNC-OAc electrocatalyst enriched with accessible FeN<sub>4</sub> active sites and hierarchically porous structure. Doping with OAc improved the density of active sites through increasing the iron content and also increase the mass transfer of the catalyst. Besides, OAc as molecular scissors could corrode carbon matrix during the carbonization process, resulting in a hierarchical pore structure. With the increase of Fe content, a small amount of Fe clusters emerges. The interaction between the FeN<sub>4</sub> site and the Fe clusters leads to a redistribution of electrons and promoting the four-electron transfer process. As a result, the obtained Fe@MNC-OAc has a high density of available single-atom iron-based active sites with significantly improved ORR activity compared to other studied iron-based catalysts and commercial Pt/C. Hence, Fe@MNC-OAc electrocatalyst prepared by this method exhibits excellent ORR performance under RRDE ( $E_{1/2}$  = 0.838 V) and PEMFC experimental conditions ( $P_{\max}$  = 903 mW cm<sup>-2</sup>). This research suggests a new approach for prepare hierarchically porous structure N-doped carbon electrocatalysts with high accessibility of active sites.

## CRediT authorship contribution statement

**Yangyang Liu:** designed the experiments, analysed the experimental data, and wrote the manuscript. **Fengdi Tu:** synthesized catalyst samples and carried out electrochemical measurements. **Ziyu Zhang and Zigang Zhao:** performed electron microscopy analyses and data interpretation. **Pan Guo and Lixiao Shen:** Data curation. **Yunlong Zhang:** Visualization, Revised the manuscript. **Lei Zhao:** Visualization, Revised the manuscript. **Guangjie Shao:** Supervision, Supplied funding for the research. **Zhenbo Wang:** Supervision, Supplied funding for the research.

## Declaration of Competing Interest

The authors declare that they have no known competing financial interests or personal relationships that could have appeared to influence the work reported in this paper.

## Data Availability

Data will be made available on request.

## Acknowledgements

This study was supported by the National Natural Science Foundation of China (Grant No. 51802059, 21905070, 22075062 and 52174281), the Shenzhen Science and Technology Program (JCYJ20210324120400002, and SGDX20210823103803017), Key Research and Development Program of Shandong Province (2022CXGC010305), Hebei Province Natural Science Foundation Innovation Group Project (B2021203016), the Hebei Key Laboratory of Applied Chemistry (22567616H), Heilongjiang Touyan Team (Grant No. HITTY-20190033), High-Level Professional Team in Shenzhen (Grant No. KQTD20210811090045006) and the Fundamental Research Funds for the Central Universities (Grant No. FRFCU5710051922).

## Appendix A. Supporting information

Supplementary data associated with this article can be found in the online version at [doi:10.1016/j.apcatb.2022.122209](https://doi.org/10.1016/j.apcatb.2022.122209).

## References

- [1] Y. Wang, D. Chen, J. Zhang, M.S. Balogun, P. Wang, Y. Tong, Y. Huang, Charge relays via dual carbon-actions on nanostructured BiVO<sub>4</sub> for high performance photoelectrochemical water splitting, *Adv. Funct. Mater.* 32 (2022), 2112738.
- [2] F. Liu, L. Shi, X. Lin, D. Yu, C. Zhang, R. Xu, D. Liu, J. Qiu, L. Dai, Site-density engineering of single-atomic iron catalysts for high-performance proton exchange membrane fuel cells, *Appl. Catal. B-Environ.* 302 (2022), 120806.
- [3] X. Lu, K.-h. Ye, S. Zhang, J. Zhang, J. Yang, Y. Huang, H. Ji, Amorphous type FeOOH modified defective BiVO<sub>4</sub> photoanodes for photoelectrochemical water oxidation, *Chem. Eng. J.* 428 (2022), 131027.
- [4] X. Xie, C. He, B. Li, Y. He, D.A. Cullen, E.C. Wegener, A.J. Kropf, U. Martinez, Y. Cheng, M.H. Engelhard, M.E. Bowden, M. Song, T. Lemmon, X.S. Li, Z. Nie, J. Liu, D.J. Myers, P. Zelenay, G. Wang, G. Wu, V. Ramani, Y. Shao, Performance enhancement and degradation mechanism identification of a single-atom Co-N-C catalyst for proton exchange membrane fuel cells, *Nat. Catal.* 3 (2020) 1044–1054.
- [5] I.E.L. Stephens, J. Rossmeisl, I. Chorkendorff, Toward sustainable fuel cells, *Science* 354 (2016) 1378–1379.
- [6] P. Guo, B. Liu, Y.-K. Dai, X.-F. Gong, Y.-F. Xia, Y.-L. Zhang, B. Liu, L. Zhao, X.-L. Sui, Z.-B. Wang, Coupling fine Pt nanoparticles and Co-N-x moiety as a synergistic bi-active site catalyst for oxygen reduction reaction in acid media, *J. Colloid Interface Sci.* 613 (2022) 276–284.
- [7] H. Zeng, S. Chen, Y.Q. Jin, J. Li, J. Song, Z. Le, G. Liang, H. Zhang, F. Xie, J. Chen, Y. Jin, X. Chen, H. Meng, Electron density modulation of metallic MoO<sub>2</sub> by Ni doping to produce excellent hydrogen evolution and oxidation activities in acid, *ACS Energy Lett.* 5 (2020) 1908–1915.
- [8] J. Song, Y.Q. Jin, L. Zhang, P. Dong, J. Li, F. Xie, H. Zhang, J. Chen, Y. Jin, H. Meng, X. Sun, Phase-separated Mo-Ni alloy for hydrogen oxidation and evolution reactions with high activity and enhanced stability, *Adv. Energy Mater.* 11 (16) (2021), 2003511.
- [9] F.A. Mashkani, H. Gharibi, M. Amani, M. Zhiani, A. Morsali, A novel electrocatalyst based on Fe-ZIF-PPY nanocomposite for oxygen reduction reaction in air-breathing direct-ethanol fuel cell, *Appl. Surf. Sci.* 584 (2022), 152529.
- [10] S.M.S. Bagheri, H. Gharibi, M. Zhiani, Introduction of a new active and stable cathode catalyst based on bimetal-organic frameworks/PPy-sheet for alkaline direct ethanol fuel cell, *Int. J. Hydrog. Energy* 47 (2022) 23552–23569.
- [11] H. Gharibi, N. Dalir, M. Jafari, M.J. Parnian, M. Zhiani, Engineering dual metal single-atom sites with the nitrogen-coordinated nonprecious catalyst for oxygen reduction reaction (ORR) in acidic electrolyte, *Appl. Surf. Sci.* 572 (2022), 151367.
- [12] M. Jafari, H. Gharibi, M.J. Parnian, M. Nasrollahpour, M. Vafaei, Iron-Nanoparticle-loaded nitrogen-doped carbon nanotube/carbon sheet composites derived from MOF as electrocatalysts for an oxygen reduction reaction, *ACS Appl. Nano Mater.* 4 (2021) 459–477.
- [13] J. Li, M.T. Sougrati, A. Zitolo, J.M. Ablett, I.C. Oguz, T. Mineva, I. Matanovic, P. Atanassov, Y. Huang, I. Zenyuk, A. Di Cicco, K. Kumar, L. Dubau, F. Maillard, G. Drazic, F. Jaouen, Identification of durable and non-durable FeNx sites in Fe-N-C materials for proton exchange membrane fuel cells, *Nat. Catal.* 4 (2021) 1.
- [14] X. Qu, Y. Han, Y. Chen, J. Lin, G. Li, J. Yang, Y. Jiang, S. Sun, Stepwise pyrolysis treatment as an efficient strategy to enhance the stability performance of Fe-Nx/C electrocatalyst towards oxygen reduction reaction and proton exchange membrane fuel cell, *Appl. Catal. B-Environ.* 295 (2021), 120311.
- [15] M. Jafari, H. Gharibi, M. Kazemi, A. Heydari, M. Zhiani, M.J. Parnian, Metal-nitrogen co-doped hierarchical porous carbon derived from the bimetallic metal-organic framework as ORR electrocatalyst for passive alkaline direct ethanol fuel cell, *J. Electroanal. Chem.* 920 (2022), 116620.
- [16] Y. He, S. Hwang, D.A. Cullen, M.A. Uddin, L. Langhorst, B. Li, S. Karakalos, A. J. Kropf, E.C. Wegener, J. Sokolowski, M. Chen, D. Myers, D. Su, K.L. More, G. Wang, S. Litster, G. Wu, Highly active atomically dispersed CoN<sub>4</sub> fuel cell cathode catalysts derived from surfactant-assisted MOFs: carbon-shell confinement strategy, *Energy Environ. Sci.* 12 (2019) 250–260.
- [17] H. Li, J. Wang, R. Qi, Y. Hu, J. Zhang, H. Zhao, J. Zhang, Y. Zhao, Enhanced Fe 3d delocalization and moderate spin polarization in Fe-Ni atomic pairs for bifunctional ORR and OER electrocatalysis, *Appl. Catal. B-Environ.* 285 (2021), 119778.
- [18] F. Tan, W. Li, J. Wang, C. Min, Z. Li, B. Zhang, X. Zheng, L. Li, L. Zhang, L. Zhou, Q. Shi, X. Yang, Clarifying the critical roles of iron in boosting oxygen reduction: Single Fe atoms anchored on carbon vacancies as efficient active sites, *Appl. Catal. B-Environ.* 305 (2022), 121035.
- [19] N.R. Sahraie, U.I. Kramm, J. Steinberg, Y. Zhang, A. Thomas, T. Reier, J.-P. Paraknowitsch, P. Strasser, Quantifying the density and utilization of active sites in non-precious metal oxygen electroreduction catalysts, *Nat. Commun.* 6 (2015) 8618.
- [20] D. Malko, A. Kucernak, T. Lopes, In situ electrochemical quantification of active sites in Fe-N/C non-precious metal catalysts, *Nat. Commun.* 7 (2016) 13285.
- [21] Q. Wang, Y. Yang, F. Sun, G. Chen, J. Wang, L. Peng, W.-T. Chen, L. Shang, J. Zhao, D. Sun-Waterhouse, T. Zhang, G.I.N. Waterhouse, Molten NaCl-Assisted synthesis of porous Fe-N-C electrocatalysts with a high density of catalytically accessible FeN<sub>4</sub> active sites and outstanding oxygen reduction reaction performance, *Adv. Energy Mater.* 11 (2021), 2100219.
- [22] A. Han, X. Wang, K. Tang, Z. Zhang, C. Ye, K. Kong, H. Hu, L. Zheng, P. Jiang, C. Zhao, Q. Zhang, D. Wang, Y. Li, An adjacent atomic platinum site enables single-atom iron with high oxygen reduction reaction performance, *Angew. Chem. -Int. Ed.* 60 (2021) 19262–19271.
- [23] X. Wan, X. Liu, Y. Li, R. Yu, L. Zheng, W. Yan, H. Wang, M. Xu, J. Shui, Fe-N-C electrocatalyst with dense active sites and efficient mass transport for high-performance proton exchange membrane fuel cells, *Nat. Catal.* 2 (2019) 259–268.

- [24] L. Zou, C.-C. Hou, Q. Wang, Y.-S. Wei, Z. Liu, J.-S. Qin, H. Pang, Q. Xu, A. Honeycomb-Like, Bulk superstructure of carbon nanosheets for electrocatalysis and energy storage, *Angew. Chem. -Int. Ed.* 59 (2020) 19627–19632.
- [25] M. Zhang, B. Yang, T. Yang, Y. Yang, Z. Xiang, A ferric citrate derived Fe-N-C electrocatalyst with stepwise pyrolysis for highly efficient oxygen reduction reaction, *Chin. Chem. Lett.* 33 (2022) 362–367.
- [26] Y. He, S. Liu, C. Priest, Q. Shi, G. Wu, Atomically dispersed metal-nitrogen-carbon catalysts for fuel cells: advances in catalyst design, electrode performance, and durability improvement, *Chem. Soc. Rev.* 49 (2020) 3484–3524.
- [27] Y. Luo, S. Fan, W. Yu, Z. Wu, D.A. Cullen, C. Liang, J. Shi, C. Su, Fabrication of Au-25(SG)(18)-ZIF-8 Nanocomposites: A Facile Strategy to Position Au-25(SG)(18) nanoclusters inside and outside ZIF-8, *Adv. Mater.* 30 (2018), 1704576.
- [28] X. Wang, Q. Li, H. Pan, Y. Lin, Y. Ke, H. Sheng, M.T. Swihart, G. Wu, Size-controlled large-diameter and few-walled carbon nanotube catalysts for oxygen reduction, *Nanoscale* 7 (2015) 20290–20298.
- [29] Y. Ye, F. Cai, H. Li, H. Wu, G. Wang, Y. Li, S. Miao, S. Xie, R. Si, J. Wang, X. Bao, Surface functionalization of ZIF-8 with ammonium ferric citrate toward high exposure of Fe-N active sites for efficient oxygen and carbon dioxide electroreduction, *Nano Energy* 38 (2017) 281–289.
- [30] J. Zhang, Z. Zhao, Z. Xia, L. Dai, A metal-free bifunctional electrocatalyst for oxygen reduction and oxygen evolution reactions, *Nat. Nanotechnol.* 10 (2015) 444–452.
- [31] D. Liu, J.-C. Li, S. Ding, Z. Lyu, S. Feng, H. Tian, C. Huyan, M. Xu, T. Li, D. Du, P. Liu, M. Shao, Y. Lin, 2D Single-atom catalyst with optimized iron sites produced by thermal melting of metal-organic frameworks for oxygen reduction reaction, *Small Methods* 4 (2020), 1900827.
- [32] Z. Zhu, H. Yin, Y. Wang, C.-H. Chuang, L. Xing, M. Dong, Y.-R. Lu, G. Casillas-Garcia, Y. Zheng, S. Chen, Y. Dou, P. Liu, Q. Cheng, H. Zhao, Coexisting single-atomic Fe and Ni sites on hierarchically ordered porous carbon as a highly efficient ORR electrocatalyst, *Adv. Mater.* 32 (2020), 2004670.
- [33] H. Huang, D. Yu, F. Hu, S.-C. Huang, J. Song, H.-Y. Chen, L.L. Li, S. Peng, Clusters induced electron redistribution to tune oxygen reduction activity of transition metal single-atom for metal-air batteries, *Angew. Chem. -Int. Ed.* 61 (2022), e202116068.
- [34] H. Shen, E. Gracia-Espino, J. Ma, H. Tang, X. Mamat, T. Wagberg, G. Hu, S. Guo, Atomically FeN<sub>2</sub> moieties dispersed on mesoporous carbon: A new atomic catalyst for efficient oxygen reduction catalysis, *Nano Energy* 35 (2017) 9–16.
- [35] Y. Cao, H. Lu, B. Xu, W. Yang, Q. Hong, Nitrogen/sulfur dual-doped porous carbon nanofibers with Co<sub>9</sub>S<sub>8</sub> nanoparticles encapsulated by graphitic shells: a highly active stable free-standing air electrode for rechargeable non-aqueous Li-O<sub>2</sub> batteries and primary alkaline Al-air batteries, *Chem. Eng. J.* 378 (2019), 122247.
- [36] L. Ma, J. Li, Z. Zhang, H. Yang, X. Mu, X. Gu, H. Jin, D. Chen, S. Yan, S. Liu, S. Mu, Atomically dispersed dual Fe centers on nitrogen-doped bamboo-like carbon nanotubes for efficient oxygen reduction, *Nano Res.* 15 (2022) 1966–1972.
- [37] J. Li, L. Jiao, E. Wegener, L.L. Richard, E. Liu, A. Zitolo, M.T. Sougrati, S. Mukerjee, Z. Zhao, Y. Huang, F. Yang, S. Zhong, H. Xu, A.J. Kropf, F. Jaouen, D.J. Myers, Q. Jia, Evolution pathway from iron compounds to Fe-1(II)-N-4 sites through gas-phase iron during pyrolysis, *J. Am. Chem. Soc.* 142 (2020) 1417–1423.
- [38] Y. Chen, S. Ji, S. Zhao, W. Chen, J. Dong, W.-C. Cheong, R. Shen, X. Wen, L. Zheng, A.I. Rykov, S. Cai, H. Tang, Z. Zhuang, C. Chen, Q. Peng, D. Wang, Y. Li, Enhanced oxygen reduction with single-atomic-site iron catalysts for a zinc-air battery and hydrogen-air fuel cell, *Nat. Commun.* 9 (2018) 5422.
- [39] Y.-j. Wu, X.-h. Wu, T.-x. Tu, P.-f. Zhang, J.-t. Li, Y. Zhou, L. Huang, S.-g. Sun, Controlled synthesis of Fe<sub>Nx</sub>-Co<sub>Nx</sub> dual active sites interfaced with metallic Co nanoparticles as bifunctional oxygen electrocatalysts for rechargeable Zn-air batteries, *Appl. Catal. B-Environ.* 278 (2020), 119259.
- [40] M. Liu, L. Wang, K. Zhao, S. Shi, Q. Shao, L. Zhang, X. Sun, Y. Zhao, J. Zhang, Atomically dispersed metal catalysts for the oxygen reduction reaction: synthesis, characterization, reaction mechanisms and electrochemical energy applications, *Energy Environ. Sci.* 12 (2019) 2890–2923.
- [41] S. Ji, Y. Chen, Q. Fu, Y. Chen, J. Dong, W. Chen, Z. Li, Y. Wang, L. Gu, W. He, C. Chen, Q. Peng, Y. Huang, X. Duan, D. Wang, C. Draxl, Y. Li, Confined pyrolysis within metal-organic frameworks to form uniform Ru-3 clusters for efficient oxidation of alcohols, *J. Am. Chem. Soc.* 139 (2017) 9795–9798.
- [42] J. Gu, M. Jian, L. Huang, Z. Sun, A. Li, Y. Pan, J. Yang, W. Wen, W. Zhou, Y. Lin, H.-J. Wang, X. Liu, L. Wang, X. Shi, X. Huang, L. Cao, S. Chen, X. Zheng, H. Pan, J. Zhu, S. Wei, W.-X. Li, J. Lu, Synergizing metal-support interactions and spatial confinement boosts dynamics of atomic nickel for hydrogenations, *Nat. Nanotechnol.* 16 (2021) 1141.
- [43] Y. Chen, S. Ji, Y. Wang, J. Dong, W. Chen, Z. Li, R. Shen, L. Zheng, Z. Zhuang, D. Wang, Y. Li, Isolated single iron atoms anchored on N-Doped porous carbon as an efficient electrocatalyst for the oxygen reduction reaction, *Angew. Chem. -Int. Ed.* 56 (2017) 6937–6941.
- [44] H. Funke, A.C. Scheinost, M. Chukalina, Wavelet analysis of extended x-ray absorption fine structure data, *Phys. Rev. B* 71 (2005) 10630–10635.
- [45] S.S.A. Shah, T. Najam, C. Cheng, L. Peng, R. Xiang, L. Zhang, J. Deng, W. Ding, Z. Wei, Exploring Fe-N-x for peroxide reduction: template-free synthesis of Fe-N-x traumatized mesoporous carbon nanotubes as an ORR catalyst in acidic and alkaline solutions, *Chem. -a Eur. J.* 24 (2018) 10630–10635.
- [46] Y. Jiang, Y.-P. Deng, R. Liang, J. Fu, D. Luo, G. Liu, J. Li, Z. Zhang, Y. Hu, Z. Chen, Multidimensional ordered bifunctional air electrode enables flash reactants shuttling for high-energy flexible Zn-Air batteries, *Adv. Energy Mater.* 9 (2019), 1900911.
- [47] Y. Lei, R. Huang, H. Xie, D. Zhang, X. Liu, Y. Si, N. Li, Electronic structure tuning of FeCo nanoparticles embedded in multi-dimensional carbon matrix for enhanced bifunctional oxygen electrocatalysis, *J. Alloy. Compd.* 853 (2021) 15707.
- [48] M. Primbs, Y. Sun, A. Roy, D. Malko, A. Mehmood, M.-T. Sougrati, P.-Y. Blanchard, G. Granozzi, T. Kosmala, G. Daniel, P. Atanassov, J. Sharman, C. Durante, A. Kucernak, D. Jones, F. Jaouen, P. Strasser, Establishing reactivity descriptors for platinum group metal (PGM)-free Fe-N-C catalysts for PEM fuel cells, *Energy Environ. Sci.* 13 (2020) 2480–2500.
- [49] L. Cao, Q. Luo, J. Chen, L. Wang, Y. Lin, H. Wang, X. Liu, X. Shen, W. Zhang, W. Liu, Z. Qi, Z. Jiang, J. Yang, T. Yao, Dynamic oxygen adsorption on single-atomic Ruthenium catalyst with high performance for acidic oxygen evolution reaction, *Nat. Commun.* 10 (2019) 4849.
- [50] L. Shen, F. Tu, Z. Shang, M. Ma, Y. Xia, Z. Zhao, L. Zhao, Z. Wang, G. Shao, Surfactant-assisted synthesis of platinum nanoparticle catalysts for proton exchange membrane fuel cells, *Int. J. Hydrog. Energy* 47 (2022) 15001–15011.